TU Delft

Delft University of Technology

Transitional flow dynamics behind a micro-ramp

Casacuberta Puig, Jordi; Groot, K.J.; Ye, Qingqing; Hickel, Stefan

Publication date
2018

Document Version
Accepted author manuscript

Published in
Proceedings of the ERCOFTAC Symposium on Engineering Turbulence Modelling and Measurement (ETMM12)

Citation (APA)
Casacuberta Puig, J., Groot, K. J., Ye, Q., & Hickel, S. (2018). Transitional flow dynamics behind a micro-ramp. In *Proceedings of the ERCOFTAC Symposium on Engineering Turbulence Modelling and Measurement (ETMM12) : 26-28 September 2018, Montpellier, France*

Important note
To cite this publication, please use the final published version (if applicable).
Please check the document version above.

Copyright
Other than for strictly personal use, it is not permitted to download, forward or distribute the text or part of it, without the consent of the author(s) and/or copyright holder(s), unless the work is under an open content license such as Creative Commons.

Takedown policy
Please contact us and provide details if you believe this document breaches copyrights.
We will remove access to the work immediately and investigate your claim.

This work is downloaded from Delft University of Technology.
For technical reasons the number of authors shown on this cover page is limited to a maximum of 10.

TRANSITIONAL FLOW DYNAMICS BEHIND A MICRO-RAMP

J. Casacuberta, K. J. Groot, Q. Ye and S. Hickel

Faculty of Aerospace Engineering, TU Delft, Kluyverweg 1, 2629HS Delft, The Netherlands

casacuberta.puig@gmail.com

Abstract

We computed the base, instantaneous and mean flow around a micro-ramp immersed in an incompressible boundary layer. Results of our Direct Numerical Simulations (DNS) are compared with an independent stability analysis and experiments. We analyse flow structures and mechanisms that contribute to the micro-ramp functionality and find that transitional perturbations increase the near-wall momentum in the mean flow more efficiently than the primary vortices in the laminar base flow.

1 Introduction

Micro-ramps are passive control devices that can reduce flow separation by increasing near-wall momentum. Their use is widespread due to their small drag penalty and structural robustness.

The wake of the micro-ramp includes a pair of counter-rotating vortices, the primary vortex pair, that alters the properties of the boundary layer and reduce its shape factor through entrainment of high-momentum fluid towards the wall (Lin, 2002; Anderson et al., 2006; Babinsky et al., 2009).

Wang et al. (2013), however, claim that the primary vortices are not capable of entraining sufficient high-momentum fluid from the free-stream to the wall while developing downstream the micro-ramp. Instead, the mechanism which makes the boundary layer fuller relies on the exchange of high- and low-momentum fluid between different portions of the boundary layer at the micro-ramp location. Li and Liu (2011) assess the performance of the micro-ramp for shock-induced separation control. A reduction of the separation bubble is not attributed to increased wall shear due to the primary vortices' motion, but to the fact that arch-shaped vortices induced at a detached shear layer weaken the shock; the micro-ramp is suggested to work differently from traditional vortex generators. Bo et al. (2012) hypothesise that the basic micro-ramp flow organisation is, at first, the consequence of the motion of the primary vortices and, thereafter, maintained by hairpin-vortex dynamics.

In this article, we present and discuss the results of DNS of the micro-ramp wake operating at incompressible conditions. There is little literature on this topic since many studies focus on micro-ramps immersed in supersonic boundary layers due to the capability of the micro-ramp to reduce shock-induced separation (Babinsky et al., 2009). A supercritical roughness Reynolds number, $Re_{hh} = u_h h/\nu$, is considered, where h denotes the micro-ramp height and u_h the streamwise velocity of the unperturbed boundary layer at this height. The micro-ramp is capable of promoting transition in these conditions. We compute and identify relevant flow structures and mechanisms present in the micro-ramp wake and analyse their influence in the generation of momentum excess. Overall, we aim to contribute to the discussion regarding the micro-ramp working principle.

The novelty of our approach lies in that, to characterise the effect of transitional perturbation development in the micro-ramp functionality, we additionally compute the laminar steady flow (the base flow) and perform a BiGlobal stability analysis of the unstable micro-ramp wake. Upon comparison between the base and the instantaneous linear and non-linear transitional flow fields, differences can be exclusively attributed to the effect of disturbance evolution.

In §2, the flow problem and the details of the DNS set-up are presented. In §3, we discuss the results of the numerical simulations: first, the topology of the base flow and the transitional flow and, secondly, the generation of momentum excess in the micro-ramp wake. In §4, we present conclusions of this article.

2 Methodology

We numerically solve the Navier-Stokes equations to determine the flow field around a micro-ramp mounted on a flat plate, in a laminar $M = 0.2$ boundary layer at $Re_{hh} = 463$. We use a computational domain of dimensions $159h \times 23h \times 46h$. DNS are performed with INCA, a Finite-Volume (FV) Immersed Boundary Method (IBM) code (Hickel et al., 2014; Örley et al., 2015) using a structured grid with 5.66×10^6 hexahedral cells and $y^+ < 1$ around all solid interfaces. To compute the steady-state of the unstable micro-ramp flow, we apply the technique of Selective Frequency Damping (SFD) (Åkervik et al., 2006; Casacuberta et al., 2018*b*). For more computational details, see Casacuberta et al. (2018*a*).

The DNS results are compared with the results of

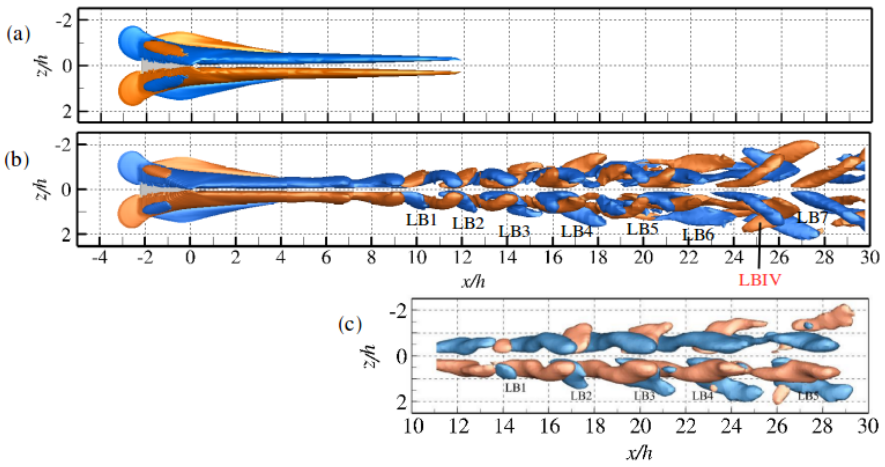

Figure 1: Instantaneous streamwise vorticity from the (a) DNS base flow, (b) DNS transitional flow, (c) PIV (Ye et al., 2018).

tomographic Particle Image Velocimetry (tomo-PIV) experiments of Ye et al. (2018) performed at the same flow conditions. The DNS results are furthermore verified by applying spatial spanwise BiGlobal stability analysis on the DNS base flow as elaborated for the experimental mean flow by Groot et al. (2016).

3 Results

Overview

The primary vortex pair induced at the micro-ramp is a key flow feature of the system's steady solution. By computing the base flow of the micro-ramp wake, we isolate the structure of the primary vortices and analyse their momentum-transport capabilities in absence of perturbation development. Figure 1(a) depicts isosurfaces of instantaneous streamwise vorticity in the base flow; the primary vortices are identified as streamwise-developing elongated symmetric structures aside the centre plane. Figure 2(a) portrays wall shear in the base flow. The imprint of the primary vortices in Figure 2(a) is evident; since they increase the near-wall momentum, symmetric regions of enhanced wall shear arise aside the micro-ramp. In line with the results of Wang et al. (2013), largest wall velocity gradients are captured near the micro-ramp. When moving downstream, wall shear exhibits a rapid decay. Figure 2(a) thus suggests that the streamwise vortex filaments are insufficient to maintain the near-wall flow energisation until the downstream region.

When SFD is not applied, perturbations leading to non-linear transitional flow arise naturally since a supercritical Re_{hh} condition is considered. Disturbance growth distorts the base flow organisation and the structure of the primary vortex pair, Figure 1(b), and alters the flow features of the near-wall region. Figure 2(b) depicts wall shear in the mean flow. By referring to the mean flow, we mean the time-averaged flow including perturbations. At a first glance, we observe major differences between the base and mean

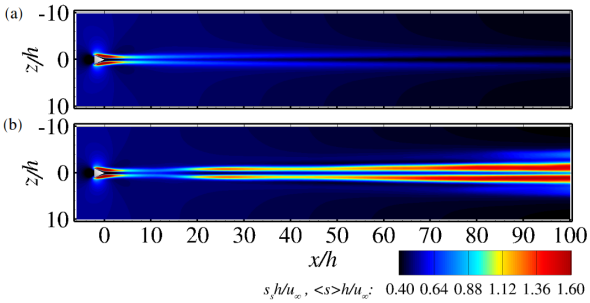

Figure 2: Wall shear in the (a) base and (b) mean flow (normalised by free-stream velocity u_∞).

wall shear manifestations sufficiently downstream the micro-ramp. From $x/h = 10$ onwards, the mean flow wall shear is enhanced significantly. Moreover, the wake of the micro-ramp in the mean flow expands in the spanwise direction. Figure 2 hence highlights the importance of the perturbation development on improving the performance of the micro-ramp in a laminar incompressible boundary layer.

In the forthcoming discussion, we first describe and analyse the base and the instantaneous flow organisations of the micro-ramp wake. Secondly, we inquire on the generation of momentum excess to explain the aforementioned differences between the base and the mean near-wall flow behaviour. The subscript "s" is used to denote base flow quantities, while mean flow variables are expressed with "$\langle\rangle$".

Organisation of the base and the transitional flow

The primary vortices are counter-rotating and induce upwash at the centre plane and a lateral downwash. The mutual vortex interaction causes them to rapidly lift off from the surface. In the base flow, the primary vortex pair is found to remain within the boundary layer at all streamwise stations. Even though the intensity of the vortices decays with x/h, as illustrated in Figure 1(a), they persist far downstream the micro-ramp. Very weak steady secondary vortices are captured as well, but these do not significantly con-

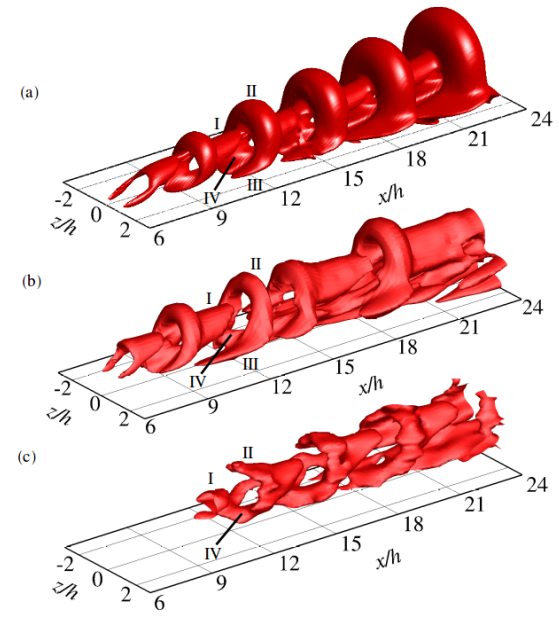

Figure 3: Streamwise-velocity perturbation from (*a*) the most unstable stability eigenfunction, (*b*) DNS, (*c*) tomo-PIV by Ye et al. (2018). Perturbation with respect to (*a*) base and (*b*,*c*) mean flow.

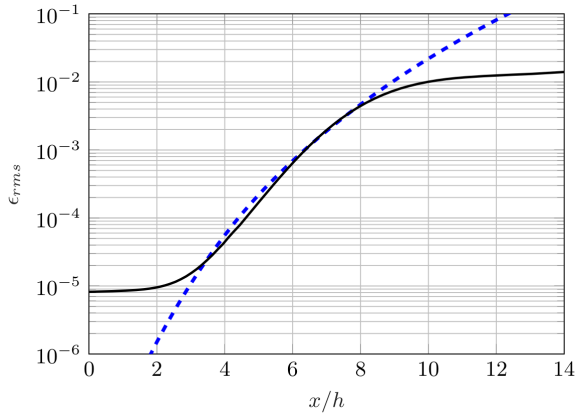

Figure 4: Streamwise velocity perturbation energy versus x/h from DNS (solid) and stability (e^{2N}, dashed).

tribute to the momentum redistribution.

A different instantaneous vortical activity is observed in the transitional flow field; see Figure 1(*b*). On the one hand, around and downstream of the micro-ramp, isosurfaces of streamwise vorticity represent the primary vortex pair. These isosurfaces show a steady behaviour and a spatial development similar to that observed in the base flow configuration. On the other hand, for increasing x/h, these structures gradually start to oscillate under the influence of perturbations. Sufficiently downstream the micro-ramp, the primary vortex pair breaks up into a train of hairpin vortices, hereafter denoted by "HP". The legs of the vortices appear as the isosurfaces of streamwise vorticity of alternating sign in Figure 1(*b*).

Stability analysis applied to the DNS base flow reveals that the wake of the micro-ramp supports two convectively unstable instabilities. The most unstable mode follows a symmetric spatial distribution. The resultant Kelvin-Helmholtz (K-H) instability leads to the formation of hairpin vortices. Figure 3 compares the streamwise velocity perturbation field obtained from instantaneous snapshots from DNS and tomo-PIV experiments (Ye et al., 2018) with the stability eigenfunction of the most unstable mode. We find a topological match between the labelled perturbation structures of Figure 3.

To quantify the perturbation growth, we compute

$$\epsilon_{rms} = \int \frac{\langle u''u'' \rangle}{u_\infty^2} \, \mathrm{d}\left(\frac{y}{h}\right) \mathrm{d}\left(\frac{z}{h}\right), \qquad (1)$$

the integrated streamwise velocity perturbation *energy*; u'' expresses an instantaneous fluctuation of streamwise velocity measured with respect to the mean flow. The streamwise evolution of ϵ_{rms} is presented in Figure 4, together with the N-factor curve obtained from the results of the stability analysis.

Close to the micro-ramp, we observe that ϵ_{rms} computed from DNS follows a plateau. It is ascribed to acoustic contamination, which sets an initial perturbation amplitude. At $x/h = 3$, DNS perturbations start to grow exponentially at the same rate as the N-factor curve. Exponential growth of disturbances is captured until $x/h \approx 9$; there, the DNS distribution bends and starts a plateau due to non-linear perturbation saturation. The disturbance energy is observed to grow again after $x/h = 14.5$, at a much lower rate.

We detect hairpins for the first time in the range $7 \leq x/h \leq 11$; see Figure 3. In this range, we additionally capture the onset of a secondary vortical structure, hereafter referred to as leg-buffer and labelled as "LB" in Figure 1(*b*,*c*). This structure was discovered by Ye et al. (2018) and we initially capture it as a protrusion of the hairpin head, referred to as a duckling beak by Groot et al. (2016). We find a good topological match between the hairpin and leg-buffer structures obtained from the results of DNS and tomo-PIV experiments in the range $x/h < 30$; see Figure 1(*b*,*c*). In turn, the leg-buffer eventually induces a tertiary vortical structure, labelled as "LBIV" in Figure 1(*b*). Despite the topological agreements, we notice differences regarding the streamwise inception location of the vortices and their wavelength. This is most probably induced by the different disturbance environment in the DNS versus the tomo-PIV experiments. Discrepancies are found as well when considering different time instants of the DNS results.

In Figure 5(*a*) and (*c*) the vertical velocity field in the planes shown in Figure 5(*b*) is depicted and furthermore the λ_2 isocontours are shown that are suggested to be responsible for the vertical velocity field.

Analysis of the momentum excess

Along the micro-ramp and at its close downstream vicinity, the action of the primary vortices highly dis-

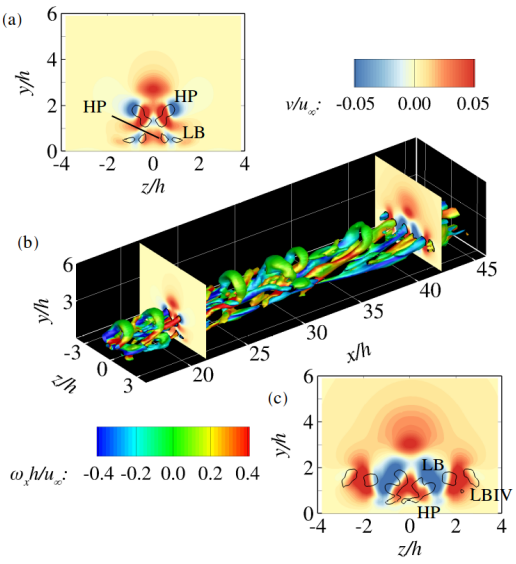

Figure 5: Instantaneous λ_2 isosurface from DNS (*b*) with y-z planes of wall-normal velocity at (*a*,*b*) $x/h = 21.5$; (*b*,*c*) $x/h = 42.2$. Isocontour of λ_2 (*a*,*c*) (black solid line).

torts the structure of the boundary layer at the micro-ramp span. High-momentum fluid from intermediate portions of the boundary layer penetrates into the low-momentum region under the action of downwash. In parallel, the upwash moves low momentum fluid from the lower portion of the boundary layer upward. Consequently, a region in which the streamwise momentum is larger than in the unperturbed boundary layer (momentum excess region) is initially generated aside the centre plane and near the surface, together with a central region in which the streamwise momentum is lower than in the unperturbed boundary layer (momentum deficit region).

The regions of momentum excess and deficit are characterised via the streamwise-velocity-streak field, the difference between the streamwise velocity and the unperturbed boundary layer: $u^{\mathrm{str}} = u - u_{\mathrm{un}}$. Figure 6 depicts planes of the base and the mean streamwise-velocity-streak field at $x/h = 20$ and 80. Close to the micro-ramp, the regions of momentum excess and deficit in the base and in the mean flow match qualitatively. However, we observe significant differences further downstream.

On the one hand, when moving downstream in the base flow, the streak field seems to diffuse. Far enough downstream, the primary vortex pair becomes incapable of maintaining the entrainment of high-momentum fluid close to the wall. This is assumed to be mainly a consequence of the initial strong lift-up of the primary vortices, together with the decreasing lateral downwash in x/h. Far downstream the micro-ramp, the regions of momentum excess have increased their area by expanding in y- and z-directions, but the near-wall fluid layers feature overall smaller values of $u_{\mathrm{s}}^{\mathrm{str}}$ than in the near-ramp field (Figure 6(*a*,*c*)).

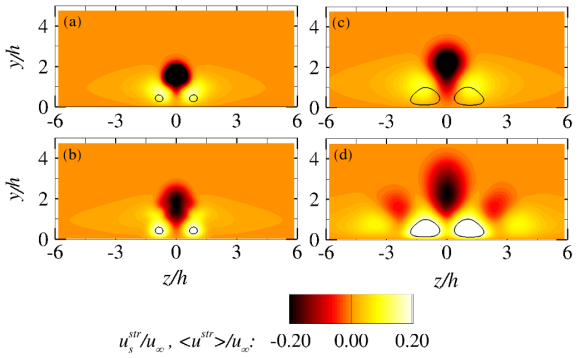

Figure 6: Streamwise-velocity streaks in the base (*a*,*c*) and mean flow (*b*,*d*) at $x/h = 20$ (*a*,*b*) and $x/h = 80$ (*c*,*d*).

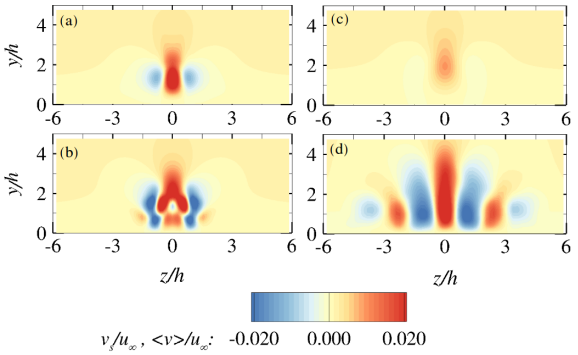

Figure 7: Wall-normal velocity in the base (*a*,*c*) and mean flow (*b*,*d*) at $x/h = 20$ (*a*,*b*) and 80 (*c*,*d*).

These results are conform with the significant decrease of the wall shear in the base flow for $x/h > 10$ illustrated in Figure 2(*a*). On the other hand, sufficiently downstream the micro-ramp in the mean flow, the lower portion of the boundary layer aside the centre plane becomes progressively fuller. Clearly, perturbations effectively entrain high-momentum fluid near the wall. The wall-normal velocity field in the base flow undergoes a strong decrease in magnitude along x/h; as illustrated in Figure 7(*a*,*c*). In the mean flow field, instead, up- and downwash regions maintain their strength and expand upward and sideward; see Figure 7(*b*,*d*). It is suggested this relative persistence is caused by the hairpins and leg-buffers in the instantaneous flow field; see Figure 5.

The perturbations enhance the redistribution of momentum and gradually modulate the mean flow boundary layer in spanwise direction. Hence, already at $x/h = 20$, the cores of the momentum excess regions in the mean flow become stronger than in the base flow (Figure 6(*a*,*b*)). Far downstream the micro-ramp, this trend is more pronounced: momentum excess in the mean flow is dominant near the wall and much stronger than in the base flow (Figure 6(*c*,*d*)). This explains the significant increase of the wall shear in the mean flow for large x/h. The largest values of $\langle u_{\mathrm{s}}^{\mathrm{str}} \rangle$ are observed at $|z/h| \approx 1$, corresponding to the spanwise location of downwash in the mean flow

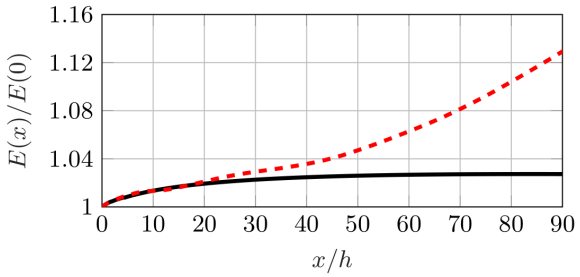

Figure 8: Evolution of the added momentum in the base (E_{B}, solid line) and mean flow (E_{M}, dashed line).

(Figures 6(*d*) and 7(*d*)). We observe further regions of added momentum aside the central ones not present in the base flow; it is suggested that these are generated solely due to the action of secondary vortices.

The aforementioned qualitative observations are quantified by evaluating the streamwise evolution of momentum excess contained in the boundary layer. For that purpose, we define

$$E_{\mathrm{B}}(x) = \int_{A^{\mathrm{E}}} \frac{\rho u_{\mathrm{s}}^{\mathrm{str}}}{\rho_\infty u_\infty} \,\mathrm{d}\left(\frac{A}{h^2}\right), \tag{2a}$$

$$E_{\mathrm{M}}(x) = \int_{A^{\mathrm{E}}} \frac{\rho \langle u^{\mathrm{str}} \rangle}{\rho_\infty u_\infty} \,\mathrm{d}\left(\frac{A}{h^2}\right), \tag{2b}$$

where E_{B} and E_{M} represent the momentum integrated over the y-z planes A^{E} where $u_{\mathrm{s}}^{\mathrm{str}}$ and $\langle u^{\mathrm{str}} \rangle$ are positive and ρ_∞ denotes the free-stream density.

Expressions (2a) and (2b) with $0 \leq x/h \leq 90$ are presented in Figure 8. In the base flow, the generation of momentum excess is not limited to the micro-ramp location, but the amount of momentum excess in the boundary layer eventually stabilises in the downstream direction. In the mean flow, from $x/h \approx 20$ onward, the amount of added momentum becomes increasingly larger, reaching a significantly higher value than in the base flow at the end of the domain.

In an attempt to quantitatively assess these differences in momentum excess generation, we derive streamwise-momentum-streak transport equations for the base and mean flow fields. We consider incompressible flow conditions and constant viscosity, which is a reasonable approximation for $M < 0.3$. In the unperturbed boundary layer, the spanwise velocity is zero ($w_{\mathrm{un}} = 0$), and the streamwise and wall-normal velocity components are independent of the spanwise coordinate ($\partial u_{\mathrm{un}}/\partial z = 0$ and $\partial v_{\mathrm{un}}/\partial z = 0$).

For characterising the momentum excess evolution, we decompose the base and instantaneous transitional flow variables as follows:

$$q_{\mathrm{s}} = q_{\mathrm{un}} + \ q_{\mathrm{s}}^{\mathrm{str}}, \tag{3a}$$

$$q \ = q_{\mathrm{un}} + \langle q^{\mathrm{str}} \rangle + q'', \tag{3b}$$

i.e. into the unperturbed boundary layer, q_{un}, the base and mean streak fields, $q_{\mathrm{s}}^{\mathrm{str}}$ and $\langle q^{\mathrm{str}} \rangle$, and unsteady fluctuations q''.

Inserting (3a) and (3b) into the steady streamwise-momentum equation, we obtain:

$$\underbrace{\rho(\boldsymbol{v}_{\mathrm{un}} \cdot \nabla) u_{\mathrm{s}}^{\mathrm{str}}}_{\textbf{streak advection}} = \underbrace{-\frac{\partial p_{\mathrm{s}}^{\mathrm{str}}}{\partial x}}_{\textbf{pressure}} + \underbrace{\mu \nabla^2 u_{\mathrm{s}}^{\mathrm{str}}}_{\textbf{diffusion}} + \underbrace{\nabla \cdot \overbrace{(-\rho u_{\mathrm{s}} \boldsymbol{v}_{\mathrm{s}}^{\mathrm{str}})}^{\textbf{streak stress}}}_{\textbf{streak-shear-correlation}}, \tag{4a}$$

$$\left.\begin{aligned} \underbrace{\rho(\boldsymbol{v}_{\mathrm{un}} \cdot \nabla) \langle u^{\mathrm{str}} \rangle}_{\textbf{streak advection}} &= \underbrace{-\frac{\partial \langle p^{\mathrm{str}} \rangle}{\partial x}}_{\textbf{pressure}} + \underbrace{\mu \nabla^2 \langle u^{\mathrm{str}} \rangle}_{\textbf{diffusion}} \\ &+ \underbrace{\nabla \cdot \overbrace{(-\rho \langle u \rangle \langle \boldsymbol{v}^{\mathrm{str}} \rangle)}^{\textbf{streak stress}}}_{\textbf{streak-shear-correlation}} + \nabla \cdot \overbrace{(-\rho \langle u'' \boldsymbol{v}'' \rangle)}^{\textbf{Reynolds stress}}, \end{aligned}\right\} \tag{4b}$$

i.e. transport equations for the base and mean momentum streaks. On the right-hand sides, besides the expected pressure and diffusion terms, we additionally obtain so-called streak-shear-correlation terms; the divergence of what hereafter will be referred to as streak stresses: $-\rho u_{\mathrm{s}} \boldsymbol{v}_{\mathrm{s}}^{\mathrm{str}}$ and $-\rho \langle u \rangle \langle \boldsymbol{v}^{\mathrm{str}} \rangle$. Equation (4b) differs from (4a) by the Reynolds stress term. Congruence between terms in Equations (4a) and (4b), especially the streak-shear correlation term, allows us to compare their relative contribution to the generation and destruction of streamwise-momentum streaks in the base and mean flow configurations.

The streamwise evolution of each of the terms in Equations (4a) and (4b) integrated over the regions of added momentum in the base and mean flow are presented in Figure 9(*a*) and 9(*b*). Each integral term characterises the relative contribution of each of the different streak transport mechanisms in the right-hand side of Equations (4a) and (4b) to the local generation of momentum excess (black squares).

Both in the base and mean flow fields, the streak stress term (blue circles) is strongly productive close to the micro-ramp, in line with Wang et al. (2013). However, in the base flow the activity of the streak stresses decays in the streamwise direction and ultimately it essentially counter-acts the effect of viscous diffusion (magenta diamonds), having a negative contribution. As a consequence, the generation of momentum excess in the base flow shows a significant decrease for large x/h compared to the near-ramp field.

In the mean flow, the contribution of the streak stresses eventually becomes increasingly positive for increasing x/h after attaining a minimum. Sufficiently downstream, perturbations take over the role of the laminar primary vortex pair in redistributing momentum within the boundary layer and start to enhance it. The curve of the streak-stress term grows enough to counter-act the negative effect of the viscous diffusion and, surprisingly, the Reynolds stresses (red solid line), and maintain the generation of momentum excess for large x/h.

4 Conclusions

We studied the wake of a micro-ramp vortex generator immersed in a boundary layer at supercriti-

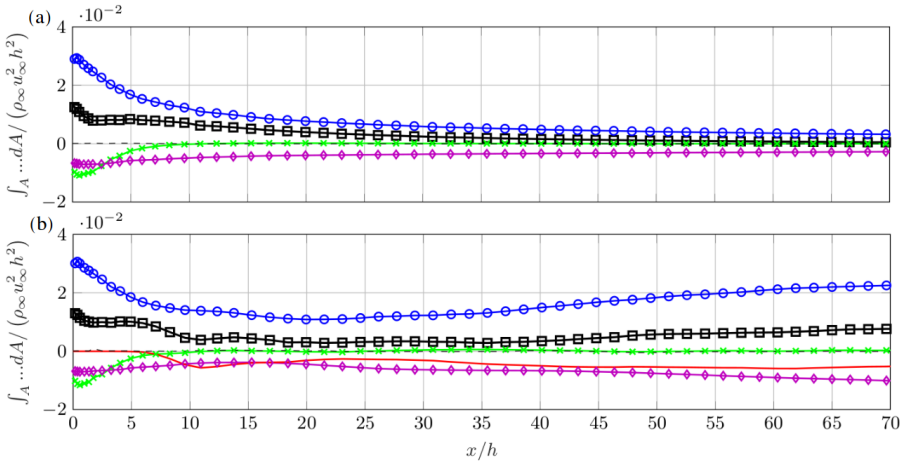

Figure 9: Streamwise evolution of the terms of (*a*) Eq. (4a) and (*b*) Eq. (4b) integrated over the regions of momentum excess in the base (*a*) and mean flow (*b*). Streak advection (black squares), streak-shear-correlation (blue circles), pressure (green crosses), diffusion (magenta diamonds), Reynolds stresses (red solid line), local sum of terms (black dashed line).

cal quasi-incompressible conditions. We performed DNS of the base, instantaneous and mean micro-ramp flow. The DNS results for the mean and instantaneous flow are in good agreement with tomo-PIV experiments at the same conditions. We furthermore performed BiGlobal stability analysis on the base flow and analysed the topology and growth rate of the instantaneous transitional vortical structures. We obtained matching linear disturbance growth rates when comparing the results of DNS and stability analysis.

There is consensus in the literature that the micro-ramp can increase the near-wall momentum and improve the "health" of the boundary layer. Nonetheless, discrepancies arise on what mechanisms cause this effect. A pair of counter-rotating vortices induced at the micro-ramp, the primary vortex pair, is the main element of the base flow. It entrains high-momentum fluid towards the wall close to the micro-ramp and decays quickly in the downstream direction. In the transitional flow field, large-scale hairpin vortices are the main instantaneous structures. Together, hairpin vortices and secondary vortices are much more effective than the primary vortices in enhancing the momentum redistribution within the boundary layer.

For the flow conditions considered in this article, we conclude that the micro-ramp does not operate as the classical vortex generator which relies on the action of downstream-evolving vortex filaments. We show that the transitional perturbations increase the near-wall momentum in the mean flow more efficiently than the primary vortices in the laminar base flow.

References

Åkervik, E., Brandt, L., Henningson, D. S., Hœpffner, J., Marxen, O. and Schlatter, P. (2006), Steady solutions of the Navier-Stokes equations by selective frequency damping, *Phys. Fluids*, Vol. 18, pp. 357-397.

Anderson, B. H., Tinapple, H. and Surber, L. (2006), Optimal control of shock wave turbulent boundary layer interactions using micro-array actuation, *AIAA Paper 2006-3197*.

Babinsky, H., Li, Y. and Pitt Ford, C. W. (2009), Micro-ramp control of supersonic oblique shock-wave/boundary-layer interactions, *AIAA J.*, Vol. 47, pp. 668-674.

Bo, W., Weidong, L., Yuxin, Z., Xiaoqiang, F. and Chao, W. (2012), Experimental investigation of the micro-ramp based shock wave and turbulent boundary layer interaction control, *Phys. Fluids*, Vol. 24, 055110.

Casacuberta, J. (2018*a*), Micro-ramp flow dynamics, MSc Thesis, TU Delft.

Casacuberta, J., Groot, K. J., Tol, H. J. and Hickel, S. (2018*b*), Effectivity and efficiency of selective frequency damping for the computation of unstable steady-state solutions, *J. Comp. Phys.*, in press.

Groot, K. J., Ye, Q., van Oudheusden, B. W., Zhang, Y. and Pinna, F. (2016), BiGlobal stability analysis of a micro-ramp wake using PIV base flows, *46th AIAA Fluid Dynamics Conference*.

Hickel, S., Egerer, C. P. and Larsson, J. (2014), Subgrid-scale modeling for implicit large eddy simulation of compressible flows and shock-turbulence interaction, *Phys. Fluids*, Vol. 26, pp. 106-101.

Li, Q. and Liu, C. (2011), Implicit LES for supersonic microramp vortex generator: new discoveries and new mechanisms, *Model. Simul. Eng.*, Vol. 2011, 15 pages.

Lin, J. C. (2002), Review of research on low-profile vortex generators to control boundary-layer separation, *Prog. Aerosp. Sci.*, Vol. 38, pp. 389-420.

Örley, F., Hickel, S., Pasquariello, V. and Adams, N. (2015), Cut-element based immersed boundary method for moving geometries in compressible liquid flows with cavitation, *J. Comp. Phys.*, Vol. 283, pp. 1-22.

Wang, X., Yan, Y., Sun, Z. and Liu, C. (2013), LES investigation into the generation of momentum deficits in the supersonic wake of a micro-ramp, *J. Mech. Sci. Technol.*, Vol. 28, pp. 1327-1337.

Ye, Q. and Schrijer, F. F. J. and Scarano (2018), F., On Reynolds number dependence of micro-ramp-induced transition, *J. Fluid Mech.*, Vol. 837, pp. 597-626.